

Nonlinearities in porous silicon optical waveguides at 1550 nm

Paveen Apiratikul¹, Andrea M. Rossi^{1,2} and Thomas E. Murphy¹

¹University of Maryland, College Park, MD 20742, USA

²Istituto Nazionale di Ricerca Metrologica, Strada delle cacce, 91 10135 Torino, Italy

paveen@umd.edu

Abstract: We report an experimental investigation of the nonlinear optical properties of nanoporous silicon optical waveguides measured at 1550 nm. The nonlinear properties including two-photon absorption, self-phase modulation, free-carrier absorption and free-carrier plasma dispersion are characterized and compared with similar measurements conducted on a conventional silicon-on-insulator ridge waveguide. Our study reveals that even waveguides that are 70% porous exhibit two-photon absorption and self-phase modulation coefficients that are comparable to those of crystalline silicon. The free-carrier absorption and dispersion in porous silicon waveguides are found to be significantly faster, and stronger than those reported for crystalline silicon.

© 2009 Optical Society of America

OCIS codes: (190.4180) Multiphoton processes; (160.4236) Nanomaterials; (160.4330) Non-linear optical materials; (190.5970) Semiconductor nonlinear optics; (190.7110) Ultrafast non-linear optics, (230.7370) Waveguides.

References and links

1. H. F. Arrand, T. M. Benson, P. Sewell, A. Loni, R. J. Bozeat, R. Arens-Fischer, M. Krüger, M. Thönissen, and H. Lüth, "The applications of porous silicon to optical waveguiding technology," *IEEE J. Sel. Top. Quantum Electron.* **4**, 975–982 (1998).
2. H. F. Arrand, T. M. Benson, A. Loni, M. G. Krüger, M. Thönissen, and H. Lüth, "Self-aligned porous silicon optical waveguides," *Electron. Lett.* **33**, 1724–1725 (1997).
3. A. Loni, L. T. Canham, M. G. Berger, R. Arens-Fischer, H. Munder, H. Lüth, H. F. Arrand, and T. M. Benson, "Porous silicon multilayer optical waveguides," *Thin Solid Films* **276**, 143–146 (1996).
4. B. Geloz and N. Koshida, "Electroluminescence with high and stable quantum efficiency and low threshold voltage from anodically oxidized thin porous silicon diode," *J. Appl. Phys.* **88**, 4319–4324 (2000).
5. J. P. Zheng, K. L. Jiao, W. P. Shen, W. A. Anderson, and H. S. Kwok, "Highly sensitive photodetector using porous silicon," *Appl. Phys. Lett.* **61**, 459–461 (1992).
6. G. Vincent, "Optical properties of porous silicon superlattices," *Appl. Phys. Lett.* **64**, 2367–2369 (1994).
7. L. Pavesi, "Porous silicon dielectric multilayers and microcavities," *Riv. Nuovo Cimento* **20**, 1–76 (1997).
8. H. F. Arrand, T. M. Benson, A. Loni, R. Arens-Fischer, M. Krüger, M. Thönissen, H. Lüth, and S. Kershaw, "Novel liquid sensor based on porous silicon optical waveguides," *IEEE Photon. Technol. Lett.* **10**, 1467–1469 (1998).
9. T. Matsumoto, M. Daimon, H. Mimura, Y. Kanemitsu, and N. Koshida, "Optically induced absorption in porous silicon and its application to logic gates," *J. Electrochem. Soc.* **142**, 3528–3533 (1995).
10. F. Z. Henari, K. Morgenstern, W. J. Blau, V. A. Karavanskii, and V. S. Dneprovskii, "Third-order optical nonlinearity and all-optical switching in porous silicon," *Appl. Phys. Lett.* **67**, 323–325 (1995).
11. F. Z. Henari, "Two photon absorption of porous silicon," *Laser Physics* **15**, 1634–1636 (2005).
12. S. Lettieri, O. Fiore, P. Maddalena, D. Ninno, G. D. Francia, and V. L. Ferrara, "Nonlinear optical refraction of free-standing porous silicon layers," *Opt. Commun.* **168**, 383–391 (1999).
13. A. M. Rossi, G. Amato, V. Camarchia, L. Boarino, and S. Borini, "High-quality porous silicon buried waveguides," *Appl. Phys. Lett.* **78**, 3003–3005 (2001).

14. T. E. Murphy, J. T. Hastings, and H. I. Smith, "Fabrication and Characterization of Narrow-Band Bragg-Reflection Filters in Silicon-on-Insulator Ridge Waveguides," *J. Lightwave Technol.* **19**, 1938–1942 (2001).
15. G. W. Rieger, K. S. Virk, and J. F. Young, "Nonlinear propagation of ultrafast 1.5 μm pulses in high-index-contrast silicon-on-insulator waveguides," *Appl. Phys. Lett.* **84**, 900–902 (2004).
16. L. Yin and G. P. Agrawal, "Impact of two-photon absorption on self-phase modulation in silicon waveguides," *Opt. Lett.* **32**, 2031–2033 (2007).
17. R. A. Soref and B. R. Bennett, "Electrooptical Effects in Silicon," *IEEE J. Quantum Electron.* **QE-23**, 123–129 (1987).
18. A. Cutolo, M. Iodice, P. Spirito, and L. Zeni, "Silicon electro-optic modulator based on a three terminal device integrated in a low-loss single-mode SOI waveguide," *J. Lightwave Technol.* **15**, 505–518 (1997).
19. G. P. Agrawal, *Nonlinear Fiber Optics, 4th ed.* (Academic Press, 2007).
20. O. Boyraz, P. Koonath, V. Raghunathan, and B. Jalali, "All optical switching and continuum generation in silicon waveguides," *Opt. Express* **12**, 4094–4102 (2004).
<http://www.opticsexpress.org/abstract.cfm?URI=OPEX-12-17-4094>.
21. M. Dinu, F. Quochi, and H. Garcia, "Third-order nonlinearities in silicon at telecom wavelengths," *Appl. Phys. Lett.* **82**, 2954–2956 (2003).
22. E. Dulkeith, Y. A. Vlasov, X. Chen, N. C. Panoiu, and R. M. Osgood, Jr., "Self-phase-modulation in submicron silicon-on-insulator photonic wires," *Opt. Express* **14**, 5524–5534 (2006).
<http://www.opticsinfobase.org/abstract.cfm?URI=oe-14-12-5524>.
23. V. R. Almeida, Q. Xu, C. A. Barrios, and M. Lipson, "Guiding and confining light in void nanostructure," *Opt. Lett.* **29**, 1209–1211 (2004).

1. Introduction

There is a growing interest in developing silicon photonics technology, for applications including optical interconnects, amplifiers, detectors, modulators and switches. Much of the research to date has focused on silicon-on-insulator ridge or channel waveguides. Porous silicon offers an interesting, although less explored, alternative to silicon-on-insulator structures.

Porous silicon is fabricated by electrochemical etching of crystalline silicon, which produces a nanoporous skeleton comprised of silicon and air. The typical pore size formed in this process ranges from 5–100 nm, depending on the etching chemistry and substrate doping. Because the pores are smaller than the optical wavelength, porous silicon behaves like an effective medium with refractive index between that of air and silicon. The refractive index depends on the porosity, which can be controlled by adjusting the electrochemical current density [1]. Complex multilayer porous structures can be fabricated by varying the current density during fabrication. Several groups have demonstrated optoelectronic devices based on porous silicon including waveguides [2, 3], LEDs [4], photodetectors [5], passive optical filters [6], microcavities [7], sensors [8] and optical switches [9].

In addition to the flexibility of a controllable refractive index, porous silicon has a number of unique properties that make it attractive for modulators and sensors. It is electrically conductive in direction perpendicular to the surface, while being optically transparent for signals polarized parallel to the surface, which could facilitate optoelectronic connectivity. As we will show here, the large internal surface area of porous silicon increases the surface recombination rate, which dramatically reduces the free-carrier lifetime.

Despite the potential applications, the nonlinear properties of porous silicon have not been extensively explored. Prior measurements of nonlinearities in porous silicon have all been performed at wavelengths below 1064 nm [10–12], where it is difficult to discern the role of free-carriers and interband absorption. To our knowledge, there has been no study of nonlinear optical properties of porous silicon in the important 1.55 μm spectral regime, and no observation of nonlinear effects in a porous waveguide. In this paper, we report the first measurement of optical nonlinearities including two-photon absorption (TPA), self-phase modulation (SPM), free-carrier absorption (FCA), free-carrier dispersion (FCD), and free-carrier lifetime in a porous silicon waveguide at telecommunication wavelengths. For comparison, we conducted similar measurements on a conventional silicon-on-insulator (SOI) ridge waveguide. We find that the

instantaneous nonlinearities (TPA and SPM) in porous silicon are comparable to crystalline silicon, but the free-carrier effects are both faster and significantly stronger in a porous silicon waveguide than in a comparable silicon waveguide.

2. Waveguide Fabrication

Porous silicon slab waveguides were fabricated by electrochemical etching of a p^{++} doped ($\sim 10^{20} \text{ cm}^{-3}$) silicon wafer in a solution of hydrofluoric acid, water and ethanol in the volume ratio (3:3:2). When forming the cladding regions, the applied current density was 400 mA/cm^2 , which was found to yield a 80% porous film with a refractive index of 1.6. The current density was temporarily reduced to 350 mA/cm^2 when etching the middle core layer, which produced a 70% porous layer with a refractive index of approximately 1.7. The refractive indices of the core and cladding layers were measured using normal-incidence spectral interferometry, performed on separately fabricated monolayer samples. This etching sequence produced a three-layer, slab waveguide comprised of a $1.8 \mu\text{m}$ thick core layer sandwiched between two lower-index cladding regions with thicknesses of 1.5 and $4.3 \mu\text{m}$, on top of a p^{++} silicon substrate. The layer thicknesses were selected based on the refractive indices to ensure single-mode operation for the slab waveguide.

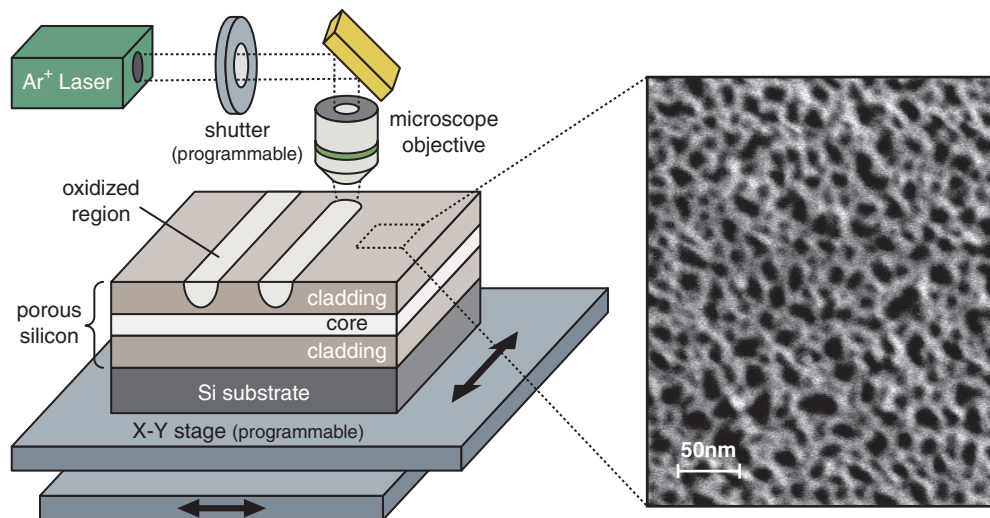


Fig. 1. Scanning laser lithography system used to produce porous silicon waveguides through a process of laser-induced oxidation [13]. The inset scanning electron micrograph shows the top-down view of the porous silicon cladding layer with 80% porosity.

After preparing the three-layer slab waveguide, a channel waveguide was patterned using the scanning laser lithography system depicted in Fig. 1 [13]. In this system, a 300 mW argon-krypton laser with wavelength of 647 nm is focused through a microscope objective onto the porous silicon sample, which causes localized heating and partial oxidation of the underlying porous silicon. The sample is then scanned beneath the focused beam to define two parallel lines, forming the left and right edges of the waveguide. The oxidized regions are then removed in a dilute hydrofluoric acid (HF) solution, forming two parallel trenches. As a final step, the entire sample is placed in an oven at 450°C for 15 minutes to produce a thin, uniform, oxide layer in order to stabilize the freshly-etched porous silicon surface.

The degree of laser-induced oxidation depends on the temperature distribution under optical illumination. While the porous silicon directly beneath the microscope objective is completely

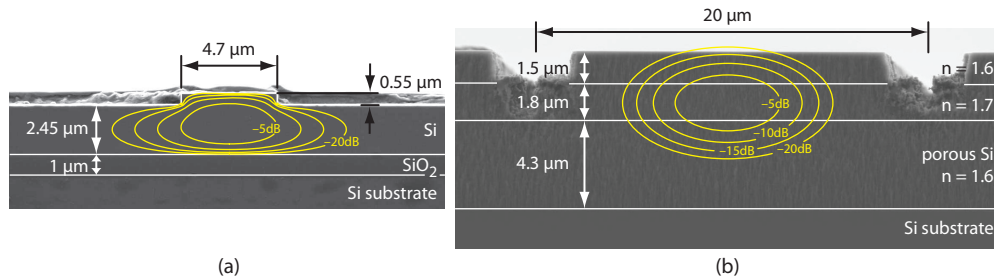


Fig. 2. Scanning electron micrographs comparing the cross sections of (a) silicon on insulator ridge waveguide and (b) porous silicon waveguide.

oxidized, the adjacent regions are only partially oxidized. Therefore, in addition to the two parallel trenches, the HF dip is also thought to produce a graded index region that confines the optical mode in a region much narrower than the inscribed lines might otherwise suggest. We fabricated waveguides with several different line spacings, and in each case observed the transmitted mode pattern on a camera for evidence of higher-order spatial modes. Waveguides wider than $20\ \mu\text{m}$ were observed to support higher-order modes, and waveguides narrow than $20\ \mu\text{m}$ suffered higher loss.

The inset scanning electron micrograph in Fig. 1 shows a top-down view of the porous cladding layer, illustrating the nanoscale texture. The pores are preferentially oriented in the out-of-plane direction (not shown), which causes significant form birefringence in the waveguide. The porous waveguide is optically transparent for TE modes that are polarized orthogonal to the pores, but highly absorbing for signals that are polarized parallel to the pores (TM modes). In this way, the heavily doped porous silicon behaves much like a wire-grid polarizer, which inhibits conductivity along the direction parallel to the wires.

For comparison, we also measured a conventional silicon-on-insulator ridge waveguide, which was fabricated using photolithography and reactive ion etching of commercially-available silicon-on-insulator substrates (for details, see [14].) Figure 2 shows cross-sectional scanning electron micrographs of the SOI ridge waveguide in comparison to the porous silicon waveguide reported here.

The mode contours that are superposed on the micrograph in Fig. 2(a) were numerically calculated using the known refractive indices and measured waveguide dimensions of the SOI ridge waveguide. Unfortunately, the refractive index profile of the porous waveguide is difficult to precisely measure, which makes numerical calculation of the optical mode challenging. The elliptical mode contours superposed on the porous waveguide in Fig. 2(b) indicate the approximate two-dimensional Gaussian mode shape, which was inferred by measuring the far-field diffraction angles of light emerging from the porous waveguide. The two micrographs are shown to scale (i.e., with identical magnification), to emphasize the similarity in mode size.

Table 1 summarizes the important linear characteristics of the two waveguides considered here. The effective index n_{eff} and loss coefficient α were estimated using a combination of Fabry Pérot spectral measurements and scattering methods. The effective area of the TE mode of the porous silicon waveguide was estimated to be approximately $2\times$ larger than that of the silicon-on-insulator waveguide.

3. Theory and Simulation

A complete description of nonlinear propagation in silicon and porous silicon waveguides must include both instantaneous nonlinear processes and free-carrier effects. The evolution of an

Table 1. Mode parameters and linear properties of SOI ridge waveguide and porous silicon waveguide.

parameter	SOI ridge waveguide	porous silicon waveguide	(unit)
n_{eff}	3.49	1.7	—
A_{eff}	10.0	19.3	(μm^2)
L	17	5.5	(mm)
α	3–5	9–13	(dB/cm)
$L_{\text{eff}} \equiv (1 - e^{-\alpha L})/\alpha$	7.5–10	2.7–3.3	(mm)
Insertion loss	20.2	15.3	(dB)

optical signal in the waveguide can be modeled by the following propagation equation [15, 16]:

$$\frac{\partial}{\partial z} u(z, t) = -\frac{\alpha}{2} u(z, t) - i \frac{\beta_2}{2} \frac{\partial^2}{\partial t^2} u(z, t) \quad (1a)$$

$$+ \left[i \frac{\omega}{c} n_2 - \frac{\beta_{\text{TPA}}}{2} \right] \frac{|u(z, t)|^2}{A_{\text{eff}}} u(z, t) \quad (1b)$$

$$- \left[i \frac{\omega}{c} \Delta n_{\text{FCD}}(z, t) + \frac{1}{2} \Delta \alpha_{\text{FCA}}(z, t) \right] u(z, t) \quad (1c)$$

where $u(z, t)$ is the slowly-varying field, normalized such that $|u(z, t)|^2$ represents the total optical power carried by the TE mode, α is the linear attenuation coefficient, β_2 describes group velocity dispersion, n_2 is the Kerr coefficient, β_{TPA} is the two-photon absorption coefficient, and A_{eff} is the effective area of the TE mode. For the simulations and experiments reported here, the dispersion β_2 was neglected because in all cases the waveguide effective length was shorter than the estimated dispersion length $L_D \equiv T_0^2/|\beta_2|$, where T_0 is the optical pulsewidth [16].

Free-carrier plasma dispersion and free-carrier absorption are described by the quantities Δn_{FCD} and $\Delta \alpha_{\text{FCA}}$ appearing in Eq. (1c), both of which are implicitly depend on the excess carrier density. For simplicity, we used a simple Drude model, in which Δn_{FCD} and $\Delta \alpha_{\text{FCA}}$ are assumed to be proportional to the excess carrier concentration ΔN :

$$\Delta \alpha_{\text{FCA}}(z, t) = \sigma_{\text{FCA}} \Delta N(z, t) \quad (2a)$$

$$\Delta n_{\text{FCD}}(z, t) = k_{\text{FCD}} \Delta N(z, t) \quad (2b)$$

where σ_{FCA} is the free-carrier absorption cross section, k_{FCD} is the free-carrier dispersion coefficient, and $\Delta N(z, t)$ is the excess carrier density, averaged over the effective mode area. To simplify the calculations, we assume that σ_{FCA} and k_{FCD} are uniform over the effective mode area, we assumed equal carrier concentrations and lifetimes for electrons and holes, and we neglected the sub-linear relationship between ΔN and Δn that has been empirically reported for holes in silicon [17, 18].

If we assume that free-carriers are generated exclusively by two-photon absorption, and that all carrier recombination processes can be described by a single time constant, then the excess carrier concentration evolves according to

$$\frac{\partial}{\partial t} \Delta N(z, t) = \frac{\beta_{\text{TPA}}}{2\hbar\omega} \left[\frac{|u(z, t)|^2}{A_{\text{eff}}} \right]^2 - \frac{\Delta N(z, t)}{\tau_c} \quad (3)$$

where τ_c is the free-carrier lifetime.

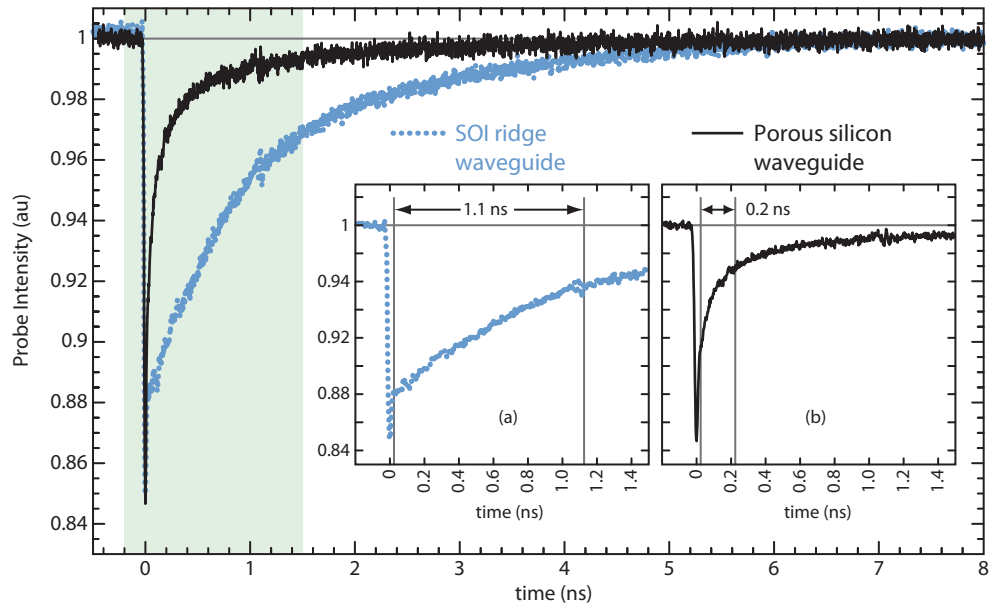


Fig. 3. Free-carrier lifetime measurements of silicon waveguide and porous silicon waveguide. Inset: (a) zoomed in plot for the silicon waveguide, and (b) zoomed in plot for the porous silicon waveguide.

Equations (1)-(3) describe two coupled nonlinear partial differential equations that must be simultaneously solved to determine $\Delta N(z, t)$ and $u(z, t)$. Although approximate analytical solutions can be formulated, in this work we numerically integrated the equations using the split-step Fourier method [19].

4. Free-carrier Lifetime

One of the key parameters that govern the operation of optoelectronic devices is the excess carrier lifetime τ_c . We measured the carrier lifetime for the two silicon waveguides using a pump-probe experiment. A Ti:sapphire-pumped optical parametric oscillator was used to deliver 150 fs pump pulses at a repetition rate of 82 MHz with center wavelength of 1490 nm, which generates free-carriers in the waveguide through two-photon absorption. The probe signal was a continuous wave, co-propagating (CW) laser with wavelength of 1560 nm. The pump and probe were combined using a beamsplitter and coupled from free-space into the waveguides using an aspheric lens. The average coupled input powers for the pump and probe were estimated to be 10 mW and 1 mW, respectively. The light emerging from the waveguide was collected using a lensed fiber and bandpass-filtered to spectrally isolate the probe signal. The probe signal was observed on a 30 GHz bandwidth optical sampling oscilloscope to monitor the transient change in transmission caused by free-carrier absorption.

Figure 3 plots the transmitted probe signals from the SOI ridge and porous silicon waveguides. The measured probe signals are normalized to their CW values in the absence of a pump pulse. In both cases, the transmitted probe exhibits a sharp, impulse-like dip followed by a slower asymptotic recovery.

The initial dip in transmission can be attributed to pump-induced two-photon absorption, i.e., simultaneous absorption of one pump photon and one probe photon. Because two-photon absorption is an ultrafast nonlinear process, the duration of this dip should closely match the

input pump pulse shape. The detector used in these measurements has 30 ps response time, which is not fast enough to resolve the depth or duration of this instantaneous dip.

The slower recovery time is attributed to optical absorption by free-carriers, which remain in the waveguide even after the pump pulse has passed. As described by Eq. (2a), the excess absorption is proportional to the carrier population, and therefore the observed recovery time in transmission gives a direct measurement of the free-carrier lifetime. The two inset figures show enlarged plots of the initial recovery. Neither time trace exhibits a purely exponential recovery, which suggests that more than one physical process contributes to the carrier recombination. Nonetheless, we obtain an estimate of the free-carrier lifetime by measuring the $1/e$ recovery time, after neglecting the initial impulse contribution from two-photon absorption. The inset figures show an enlarged view of the first 1.5 ns after arrival of the pump pulse. The SOI ridge waveguide exhibits a carrier lifetime of approximately 1.1 ns, which is comparable to prior measurements conducted on silicon waveguides [20]. The porous silicon waveguide, which has a comparable mode area to the SOI waveguide, exhibits a much more rapid recovery time of 200 ps. The faster free-carrier lifetime in porous silicon could be explained by the much higher surface recombination rate in the nanoporous material as well as the much faster Auger recombination lifetime in the heavily doped material. We believe the diffusion does not play an important role in reducing the free-carrier lifetime in the porous silicon waveguide since the diffusion length is likely to be shorter than the waveguide dimensions. We note that in both cases, the observed carrier lifetime is much shorter than the repetition rate of the pump laser, which allows us to neglect the cumulative buildup of free-carriers generated by prior pulses.

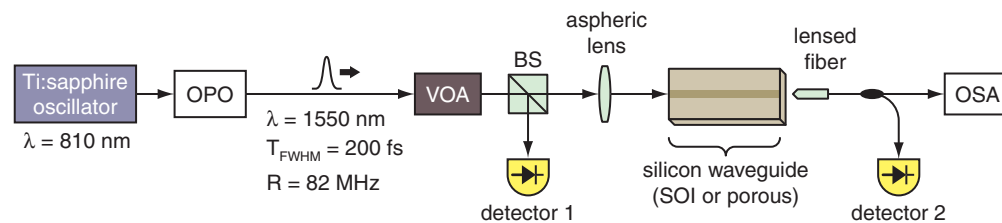


Fig. 4. Experimental setup for measuring optical nonlinear parameters in SOI waveguides and porous silicon waveguides.

5. Nonlinear Measurements

The instantaneous and carrier-based nonlinear properties were determined by launching pulses into the waveguide and measuring the output power and output spectrum as a function of the input optical power. For low input power, the output power is directly proportional to the input power and the output spectrum has the same shape as the input spectrum. As the input power is increased, the ratio of transmitted to input power decreases as a result of two-photon absorption and free-carrier absorption. Similarly, at higher input power, the output spectrum broadens and shifts as a result of the self-phase modulation and free-carrier dispersion.

Figure 4 depicts the experimental setup used to observe these nonlinear effects. The input pulses were generated using a Ti:sapphire-pumped optical parametric oscillator, which produced transform-limited 200 fs pulses with a center frequency of 1550 nm and repetition rate of 82 MHz. The input power was adjusted using a variable attenuator, and coupled from free space into the waveguide through a high numerical aperture aspheric lens. In all measurements, the input polarization state was adjusted to excite only the TE mode of the waveguide. The light emerging from the waveguide was collected using a tapered single-mode optical fiber and directed to either an optical spectrum analyzer or power meter.

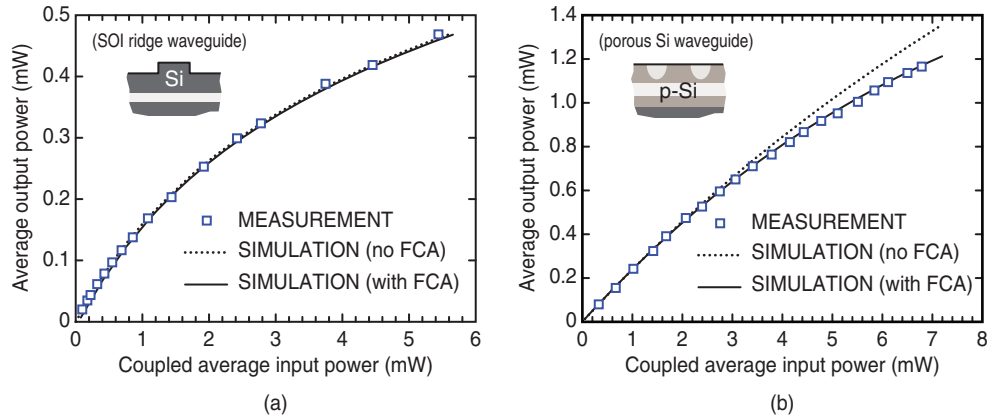


Fig. 5. Output power vs. input coupled power (a) for the SOI ridge waveguide waveguide and (b) for the porous silicon waveguide considered here. The open squares indicate the measured data, whereas the curves show theoretical fits obtained from numerical simulation. The dashed curves indicate the fit obtained by neglecting free carrier effects, whereas the solid curves includes both two-photon absorption and free-carrier absorption.

5.1. Nonlinear Absorption

The open squares in Fig. 5(a) show the measured output power vs. input power for the SOI ridge waveguide depicted in Fig. 2(a). For this waveguide, the maximum average coupled input power was 5.4 mW, which corresponds to an average intensity of 3 GW/cm². The power transmission ratio decreases at higher input power, as evidenced by the downward curvature in the plot of P_{out} vs. P_{in} . The theoretical curves shown in Fig. 5(a) were obtained by numerically solving Eqs. (1)-(3). When performing the numerical simulations, we used previously measured values for α , and adjusted β_{TPA} and σ_{FCA} in order to best fit the experimental measurements.

In the SOI waveguide, we found that at the optical intensities considered here, the nonlinear relationship between P_{out} vs. P_{in} can be almost entirely described by instantaneous two-photon absorption. The dashed curve shown in Fig. 5(a) was obtained by neglecting free-carrier absorption in the simulation (i.e., by setting $\sigma_{\text{FCA}} = 0$), which gives results that are almost indistinguishable from the solid curve, which used the previously reported value $\sigma_{\text{FCA}} = 1.45 \times 10^{-17}$ cm² [18]. We therefore conclude that for the SOI waveguide, the measurement of P_{out} vs. P_{in} alone does not permit accurate determination of the free-carrier absorption cross section. By fitting the simulations and experiments, we estimated the two-photon absorption coefficient of silicon to be $\beta_{\text{TPA}} = 1 \pm 0.25$ cm/GW, which is consistent with previously reported measurements in silicon [15, 21]. The uncertainty in our estimate of β_{TPA} is primarily attributed to uncertainty in the coupling efficiencies at the input and output facets.

Figure 5(b) shows a similar measurement performed on the porous silicon waveguide shown in Fig. 2(b). In this case, the maximum attainable average coupled input power was 7 mW, which corresponds to an average intensity of 2 GW/cm². As with the SOI ridge waveguide, the power transmission ratio decreases at high intensity due to nonlinear absorption. In this case, however, the measured data cannot be explained without including free-carrier absorption. The dashed curve shows a best-fit simulation neglecting free-carrier absorption, whereas the solid curve includes both two-photon absorption and free-carrier absorption, and gives excellent agreement with the observations. From this fit, the TPA coefficient and free-carrier absorption cross section in porous silicon waveguide were estimated to be 0.8 ± 0.1 cm/GW and $(100 \pm 20) \times 10^{-17}$ cm², respectively. Even though the waveguides are 70-80% porous,

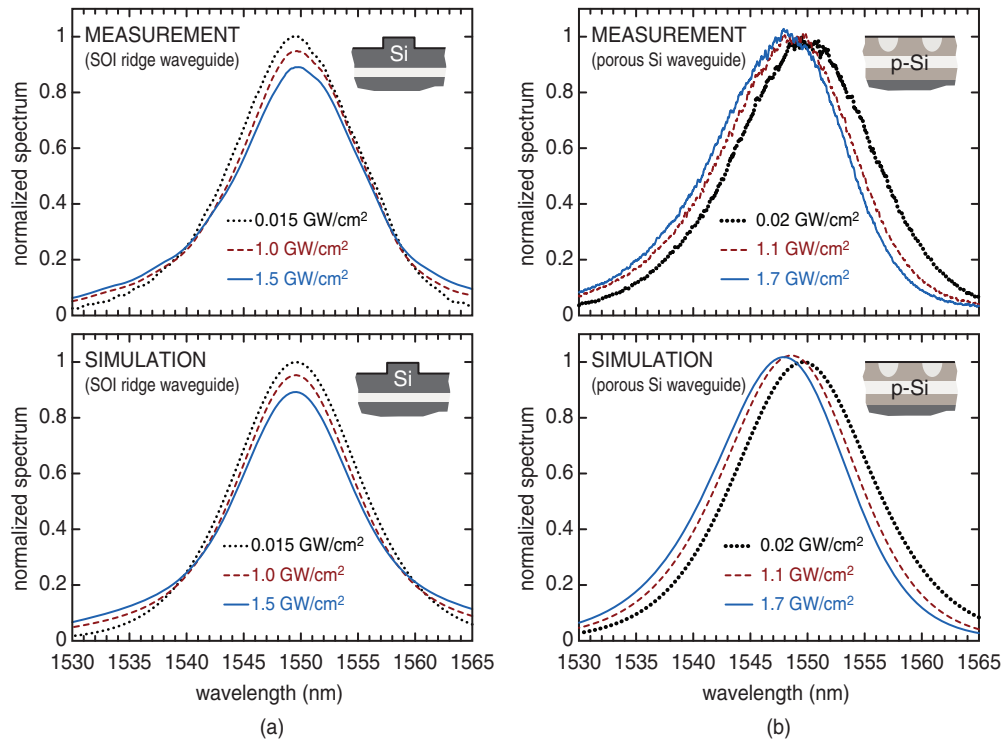


Fig. 6. (a) Upper: Experimentally measured output spectra for three different input intensities for the SOI ridge waveguide, showing spectral broadening caused by self-phase modulation. Lower: Corresponding numerical simulations used to match the measurements. (b) Upper: Experimentally measured output spectra for three different input intensities, for the porous silicon waveguide, showing blue-shift associated with free-carrier dispersion. Lower: Corresponding numerical simulations.

the TPA coefficient in porous silicon is only slightly lower than the value in silicon. Surprisingly, the free-carrier absorption cross section in porous silicon waveguide is approximately two-orders-of-magnitude larger than what is reported for bulk silicon [18], as summarized in Table 2. The anomalously high free-carrier cross section could be explained by the higher collision frequency due to the lower mobility of the heavily-doped porous silicon skeleton.

5.2. Nonlinear Refraction

Figure 6(a) plots the measured (upper) and simulated (lower) output optical spectrum from the SOI ridge waveguide, measured for three different input intensities. The input intensities were calculated based on the coupled input power and effective mode area of the SOI waveguide. In order to better compare the spectral shapes, all three of the spectra were normalized to have the same total area. As the input intensity is increased, the output spectrum broadens slightly as a result of self-phase modulation. The spectral broadening can be entirely described by the inclusion of self-phase modulation (n_2) in the simulation. As with the nonlinear absorption measurements, the inclusion of free-carrier effects in the model was found to have no clearly discernable effect on the simulated spectra, for the parameters considered here. By matching simulations and measurements, we estimated nonlinear refractive index for silicon to be $n_2 = (4.2 \pm 0.8) \times 10^{-14} \text{ cm}^2/\text{W}$, which agrees with the results reported in the literature [21,22].

Table 2. Comparison of nonlinear properties measured from crystalline SOI ridge waveguide and porous silicon waveguide.

parameter	SOI ridge waveguide	porous silicon waveguide	(unit)
τ_c	1.1	0.2	(ns)
β_{TPA}	1 ± 0.25	0.8 ± 0.1	(cm/GW)
n_2	4.2 ± 0.8	2.3 ± 0.7	($\times 10^{-14}$ cm ² /W)
σ_{FCA}	1.45 ^a	100 ± 20	($\times 10^{-17}$ cm ²)
k_{FCD}	3.5–7.5 ^b	90 ± 15	($\times 10^{-21}$ cm ³)

^a For the SOI ridge waveguide, the value of σ_{FCA} could not be reliably estimated from our measurements. For comparison, we tabulate here the accepted value of σ_{FCA} for crystalline silicon, as reported in the literature [17, 18].

^b For the SOI ridge waveguide considered here, the value of k_{FCD} was too small to be reliably determined from our measurements. The range tabulated here was calculated using the empirical model given in [18], for carrier concentrations in the range 10^{15} – 10^{17} cm⁻³.

Figure 6(b) plots similar spectral measurements (upper) and simulations (lower) for the porous silicon waveguide considered here. In this case, the spectrum exhibits a pronounced blue shift at higher input intensities, which is a signature of free-carrier dispersion. By fitting the blue-shift to the theoretical models, we determined the free-carrier dispersion coefficient to be $k_{\text{FCD}} = (90 \pm 15) \times 10^{-21}$ cm³. As indicated in Table 2, this figure is more than an order of magnitude higher than what is reported for crystalline silicon [17, 18].

Aside from the blue-shift, the spectrum shows very little change in width as the power is increased, which suggests the self-phase modulation does not play an important role. However, through a careful analysis we found that the simulations cannot be made to match the experiments without including self-phase modulation terms (n_2). If SPM terms are neglected, but two-photon absorption terms are included, then the spectrum would become narrower at higher intensities, as a result of TPA-induced pulsewidth spreading. The inclusion of SPM causes spectral broadening which counteracts the spectral narrowing caused by TPA. By modeling both effects, we were able to match the experimentally observed spectra, from which we estimate the nonlinear refractive index of porous silicon to be $n_2 = (2.3 \pm 0.7) \times 10^{-14}$ cm²/W. We emphasize that this estimate requires finding a self-consistent fit to both the spectral measurements in Fig. 6(b) and the transmission measurements in Fig. 5(b). Despite a high porosity of 70-80%, the porous silicon exhibits a nonlinear refractive index that is comparable in magnitude to that of crystalline silicon, as summarized in Table 2.

6. Conclusions

We report here the first experimental measurement of the instantaneous and carrier-based nonlinear effects in porous silicon waveguides at 1550 nm. We used a combination of three different measurements: pump-probe transient absorption, nonlinear changes in the transmitted power and nonlinear changes in the transmitted spectrum. By matching these measurements against numerical simulations, we estimated the coefficients that describe two-photon absorption, self-phase modulation, free-carrier absorption, free-carrier dispersion, and carrier lifetime. For comparison, and to confirm the credibility of our models, we conducted identical measurements on a conventional silicon-on-insulator ridge waveguide, which gave results consistent with those that have been reported in the literature.

The instantaneous nonlinear parameters that describe self-phase modulation and two-photon absorption (n_2 and β_{TPA}) in porous silicon were found to be comparable in magnitude to those reported in the literature (and confirmed by our measurements) for crystalline silicon waveguide.

uities. These results are surprising because the porous waveguides considered here are comprised of 70–80% air and only 20–30% silicon, and for the TE-polarized mode, the optical mode is expected to strongly concentrate in the low-index air voids [23].

The carrier-based nonlinearities in porous silicon are markedly stronger and faster in porous silicon, compared to what has been reported for crystalline silicon. The carrier lifetime in porous silicon is significantly shorter than in conventional silicon waveguides, which we attribute to the very high surface-area of the nanoporous skeleton. The Drude coefficients that best describe the plasma dispersion effect in porous silicon are found to be much larger than what has been reported earlier for crystalline silicon. The physical origin of this anomaly merits further investigation, but it could be related to the dramatically altered mobility in nanoscale composites, or the high doping concentration of the porous silicon used here.

These results suggest that porous silicon could be an interesting alternative to crystalline silicon for future applications in all-optical switching or fast electrooptic modulators.

Acknowledgments

This work was supported in part by the National Science Foundation (NSF) under CAREER Grant 0546928. We would also like to acknowledge the support of the Laboratory for Physical Sciences and the Maryland Nanocenter.